Fuel 319 (2022) 123748

Contents lists available at ScienceDirect

Fuel

journal homepage: www.elsevier.com/locate/fuel

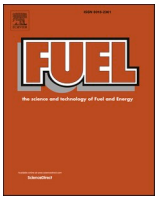

Analysis of a newly developed locomotive engine employing sustainable fuel blends with hydrogen

Shaimaa Seyam *, Ibrahim Dincer, Martin Agelin-Chaab

Clean Energy Research Laboratory (CERL), Ontario Tech University, Oshawa, Ontario L1G 0C5, Canada

ARTICLE INFO

Keywords:
Hydrogen
Locomotive engine
Solid oxide fuel cell
Proton exchange membrane fuel cell
Fuels
Sustainability

ABSTRACT

Transportation emissions from fossil fuels and low efficiency engines significantly contribute to global warming. One way to mitigate this is to develop more efficient engines and use sustainable fuels. This paper presents a novel hybrid locomotive engine to replace the EMD 16-710G3 engine used for Canada's rail transportation. It consists of a gas turbine instead of an internal combustion engine, solid oxide fuel cell with steam reformer and water gas shift reactor, and thermoelectric generator and absorption refrigeration system for energy recovery, and onboard hydrogen production using aluminum electrolysis cell and proton exchange membrane fuel cell. The used fuels are methanol, hydrogen, methane, ethanol, and dimethyl ether rather than diesel fuel. This integrated system is investigated thermodynamically to evaluate the energy performance. The system performance is increased from 40% to 48% and 50% of energy and exergetic efficiencies, while the total power is increased from 3383 kW to 7211 kW using a methane and hydrogen blended fuel. Also, the engine has an efficiency above 60% using a dimethyl ether and hydrogen blend. Using alternative fuels helps reduce CO_2 emissions by 50% for the methane and hydrogen blend and more than 70% for the other blends, such as ethanol and dimethyl ether blended with hydrogen. The proposed engine can potentially be applied to improve the overall system performance and reduce the environmental impact.

1. Introduction

In the last two years, the world has been affected by the COVID-19 pandemic and its different mutations that caused many fatalities. Many studies have linked this disease with carbon emissions and global warming [1–4]. The transportation sector has contributed significantly to global warming. As reported in Natural Resources Canada of 2021–2022, the transportation sector emitted about 130 Mt of CO_2 eq. in 2000 and this increased to 180 Mt of CO_2 eq. in 2020 which is about 38% [5] due to the large transportation use of oil and fossil fuels. Such huge amounts of emissions must be reduced by introducing new powering systems and using sustainable fuels instead of fossil fuels.

Fuel cells are incorporated with powering systems to produce electricity through electrochemical reactions by passing electrons between electrodes to produce ions: such as hydrogen ions as in proton exchange membrane fuel cell (PEMFC), oxygen ions, as in solid oxide fuel cell (SOFC), and carbonate ions, as in molten carbonate fuel cell (MCFC) [6]. Fuel cells can be hybridized with batteries in rail transportation. For example, Akhoundzadeh et al. [7] investigated a hybrid train that is powered by lithium-ion battery and PEMFC using hydrogen fuel with different ratios for diesel multiple unit (DMU) rail commuter. They found that high levels of fidelity can be achieved with acceptable fuel cell sizes and shared power with battery after the authors investigated the time response, controllers, split power, and velocity dynamics, and tested different scenarios. Also, Sarma and Ganguly [8] presented a hybrid electric commuter comprising of a PEMFC and a battery. They optimized their system to approach optimal size with optimal operating conditions and split power. In addition, fuel cells can be combined with a steam reformer (SR) and a water gas shift reactor (WGSR) as a compact unit, so the fuel cells can operate with many fuels and can be used in transportation engines. For example, Seyam et al. [9] designed an integrated locomotive engine consisting of internal combustion engine (ICE), MCFC, and a gas turbine (GT) utilizing sustainable fuels to increase the overall engine power to 25% with higher performance of 43% and 55% of thermal (energy) and exergetic efficiencies, respectively, and reduced the CO_2 emissions by more than 60%. Al-Hamed and Dincer [10] presented a novel powering system for a locomotive including a SOFC and a PEMFC combined with a GT engine using ammonia fuel. The waste energy of exhaust gases was utilized in ammonia dissociation and

* Corresponding author.
E-mail addresses: Shaimaa.seyam@ontariotechu.net (S. Seyam), Ibrahim.dincer@ontariotechu.ca (I. Dincer), Martin.agelin-chaab@ontariotechu.ca (M. Agelin-Chaab).

https://doi.org/10.1016/j.fuel.2022.123748
Received 4 January 2022; Received in revised form 12 February 2022; Accepted 1 March 2022
Available online 29 March 2022

Nomenclature

Symbols

A	area [cm^2]
E	Nernst voltage [V]
$\dot{E}$	energy rate [kW]
$\dot{Ex}$	exergy flow [kw]
F	Faraday constant [C/mol]
$\overline{g}$	Gibbs free energy [kJ/mol]
h	specific enthalpy [kJ/kg]
i	current density [A/cm^2]
I	thermoelectric current [A]
K	thermal conductance [W/(m.K)]
N	number of cells/ stacks
$\dot{m}$	mass flow rate [kg/s]
P	pressure [kPa]
$\dot{Q}$	heat rate [kW]
r	electric resistance [Ω]
R	resistive loss [$\Omega - cm^2$]
$\overline{R}$	molar gas constant [J/mol.K]
s	specific entropy [kJ/(kg.K)]
T	temperature [K]
V	voltage [V]
$\dot{W}$	power, work rate [kW]

Abbreviations

AEC	ammonia electrolysis cell
BR	afterburner
C	compressor
CC	combustion chamber
PEMFC	proton exchange membrane fuel cell
SOFC	solid oxide fuel cell
SR	steam reforming
T	turbine
TG	thermoelectric generator
WGS	water gas shift

Subscripts

an	anode
ca	cathode
D	destruction
e	electrical
t	total, overall

Greek letters

ψ	exergetic efficiency [%]
η	thermal (energy) efficiency [%]
δ	thickness [μm]
$\boldsymbol{\epsilon}$	porosity [-]

separation unit for on-board hydrogen production and a heating load for a steam Rankine cycle and ammonia-organic Rankine cycle. The overall performance increased to 60% and 66% thermal and exergetic efficiencies, respectively. In another study, Guo et al. [11] designed a combined system of a GT of the turbofan engine and SOFC. The fuel is selected to be ammonia and water mixture, which is flowing to an Al-H_2O reactor for hydrogen production that is used in SOFC to produce electricity. The exhaust of the SOFC enters the combustion chamber of the GT for a complete combustion. This integration increased its performance by reducing the fuel consumption of the GT by about 20% and also increased the power generation by 25%.

Using hydrogen fuel as a sustainable and green fuel with free carbon emission has proven its benefits by increasing the performance of engines. However, hydrogen storage is a crucial barrier to many applications. Therefore, onboard hydrogen production can be a solution to such a problem using aluminum electrolysis cells (AEC). This AEC can be employed by electrochemical reactions of pure liquid aluminum to dissociate into amide ions (NH_2^-) and ammonium ion (NH_4^+) by adding amide salts such as (KNH_2, $LiNH_2$, or $NaNH_2$) as reported by [12,13]. This cell can decompose ammonia into hydrogen and nitrogen with a molar ratio of 3.26 and release 6.715×10^{-3} mol of hydrogen. Another experiment was performed by Goshome et al. [14], where 5 M of solid NH_4Cl was dissolved in liquid ammonia to dissociate liquid ammonia into NH_2^- andNH_4^+, but NH_4^+ was reduced on the cathode electrode to produce hydrogen gas, while the ammonia was oxidized to produce nitrogen gas. If the liquid ammonia is not available because of its high prices, ammonia-water solution can also be used in AEC. For example, Hanada et al. [15] established an experimental setup of 50 ml solution of 1 M of NH_3 and 1 M of KOH to be dissolved in it. The presence of KOH is to alkalize the water to produce OH^- and hydrogen at the cathode, and the ammonia is oxidized with hydroxide to produce nitrogen gas.

Waste energy from engines worries many manufacturers and researchers as well. It can be utilized in useful energy such as power generation of cooling loads. Another way for such a technique is to use a thermoelectric generator (TG). Luo et al. [16] have applied TG modules in automobile waste heat recovery. The TG can produce electricity of about 40 W at a vehicle speed of 120 km/h. The TG can also be applied to geothermal pipes. Alegria et al. [17] have designed a small model of a geothermal pipe attached to TG models. The resultant power was obtained to be 10 to 20 W; however, the heat transferred is about 330 to 480 W and the hot temperature was in the range of 100 ℃ to 160 ℃. Also, Ma et al. [18] built a platform of 32 TG models attached to an exhaust pipe. The inlet mass flow rate varied from 12 to 24 kg/h and inlet temperature changed from 100 ℃ to 300℃. The TG power was obtained to be 0.66 to 3.17 W with an efficiency of 0.67%. In addition, Chen et al. [19] established an integrated system of MCFC and TG with an inhomogeneous heat conduction and regenerator to employ the waste heat of MCFC and convert it to electric power. The overall power increased by 35% resulting in an increase in the overall efficiency by 7% compared to the MCFC only.

The main objective of the current paper is to propose a newly designed hybrid locomotive engine with onboard hydrogen production, and a new energy recovery system to replace the EMD 16-710G3 of 3355 kW for Canadian rail transportation [20]. This paper also studies the performance of the presently designed energy system by means of thermodynamic tools and compares its performance to the traditional engine system. In addition, the designed system is operated using five sustainable fuels with five blending ratios to measure the environmental impact of the proposed design. Furthermore, some parametric studies are conducted to select better operating conditions for best performance.

2. System description

The hybrid locomotive engine is designed as shown in Fig. 1. This hybrid engine consists of three subsystems working together with another auxiliary system for hydrogen production. The hybrid engine composes of the following: gas turbine (GT) comprising of a compressor (C1), a combustion chamber (CC), and a turbine (T1); a SOFC system comprising of a steam reforming (SR), a water gas shift (WGS), SOFC units, and afterburner (BR); and energy recovery system comprising of a thermal generator (TG) and an absorption refrigeration system (ARS).

The intake air is compressed by C1 and used in the combustion with fuel blends and expanded by T1 to be exhausted to the atmosphere. The exhaust gas releases the GT system at a very high temperature with high

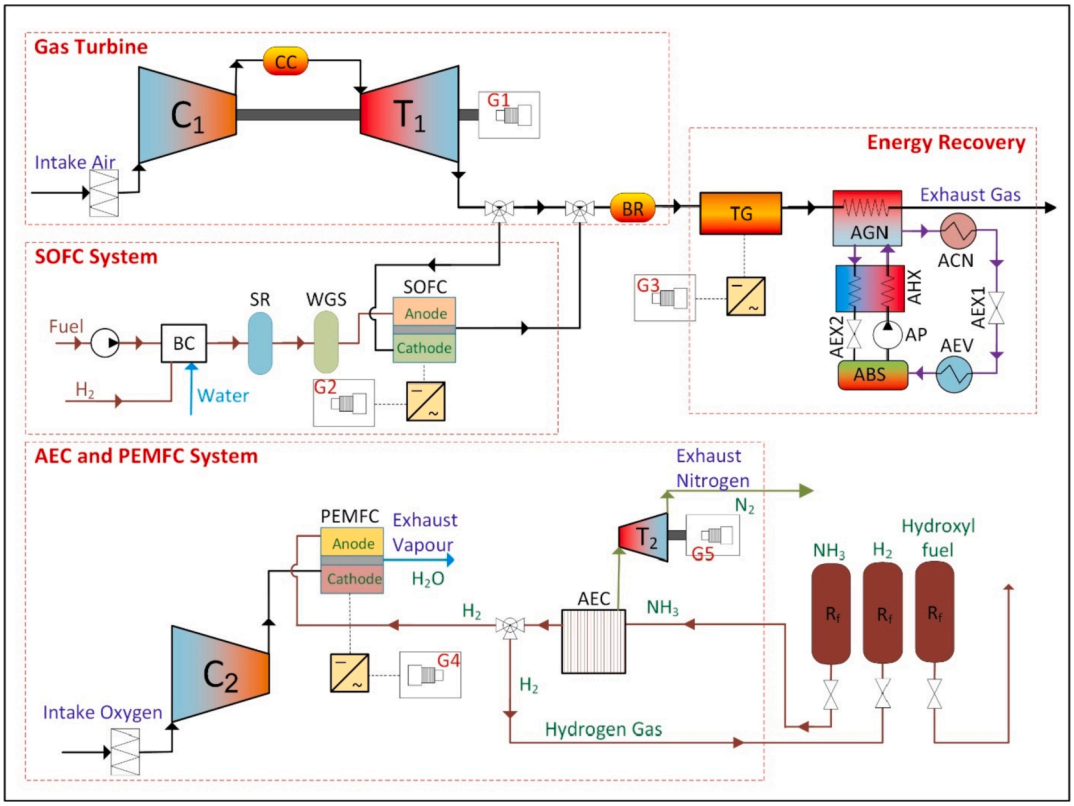

Fig. 1. Schematic diagram of the hybrid locomotive engine.

emissions as well. Therefore, the exhaust gas is split to enter the SOFC system which also uses a mixture of fuel blend and water to be reformed and electrochemically transformed into steam to produce electricity. Any unburned fuels will be completely re-combusted in the BR at lower temperature than the exit of the turbine. The exhaust gases still have excessive heat which can be transformed into electricity by the TG and the cooling load by ARS.

The hydrogen production system is executed on board the train separated from the engine to refill to store the hydrogen fuel. This system consists of an aluminum electrolysis cell that used aluminum solution and potassium hydroxide solution to produce two gases: hydrogen and nitrogen gases. The nitrogen gases are released to the atmosphere after expanding by T2. Some of the hydrogen can be stored, the remaining hydrogen can be used for electrochemical reactions of PEMFC with compressed oxygen by C2 to produce a hot steam and electricity.

This hybrid system can be modelled using Aspen Plus, which is a powerful tool for simulating the thermodynamics and chemical reactions of systems. The flowcharts are presented separately for each system in Fig. 2, showing the stream numbers and component names.

3. Methodology

The newly designed engine is modelled and analyzed thermodynamically to present the energetic efficiency and exergetic efficiency of the system. The following subsections discuss the thermodynamic modeling for each subsystem.

3.1. System modeling

The hybrid locomotive engine is operated by a turbomachinery engine of a gas turbine (GT) comprising of a compressor, a combustion chamber, and a turbine. The specifications of the gas turbine are listed in Table 1. The GT's resultant power is estimated by:.

$$\dot{W}_{GT} = \dot{W}_{T1} - \dot{W}_{C1} \tag{1}$$

The CC heat addition is expressed as the following:.

$$\dot{Q}_{CC} = \dot{m}_{B3}h_{B3} - \dot{m}_{F1}h_{F1} - \dot{m}_{B2}h_{B2} = \eta_{CC}\dot{m}_{F1}LHV_{F1} \tag{2}$$

The performance of the GT can be measured by evaluating thermal efficiency (η_{GT}) and exergetic efficiency (ψ_{GT}), which are presented below:.

$$\eta_{GT} = \frac{\dot{W}_{GT}}{\dot{Q}_{CC}} \text{ and } \psi_{GT} = \frac{\dot{W}_{GT}}{\dot{E}x^{Q}_{CC}} \tag{3}$$

3.2. Modeling of fuel cells

The fuel cells of AEC, PEMFC, and SOFC are electrochemical systems that generates electric power from the electrochemical reactions or uses electric power to produce fuel. These systems are characterized as fossil fuel free, less emission, less energy loss, and high electric efficiency. They are also considered as no mechanical movement, which require less maintenance, and produce less noise. This section displays modeling of the SOFC, PEMFC, and AEC cells showing the thermal and electrical modeling. The specifications of fuel cells are listed in Table 2.

3.2.1. Solid oxide fuel cell (SOFC)

The SOFC is an electrochemical device that generates electricity by oxidizing a fuel using solid oxide material. The SOFC consists of two porous electrodes of anode, which is made of Ni-ZrO_2 or Co-ZrO_2 cermet and cathode, which is made of Strontium doped Lanthanum Manganate ($LaMnO_3$). These electrodes are separated dense oxide ion conducting electrolyte, which is fabricated by Yttria stabilized with zirconia [22]. The fuel blends mix with water before flowing to the SOFC system, which must be steam reformed by the SR and water shifted by the WGS to produce hydrogen gas that enters the anode. The H_2 will electrochemically react with oxygen ions that are produced by the cathode and

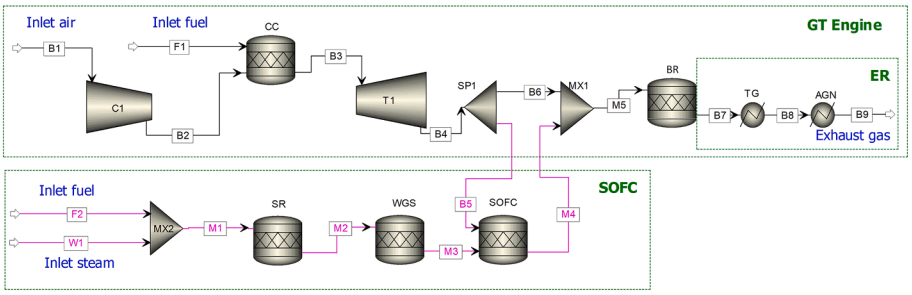

(a) Flowchart for the GT and SOFC systems

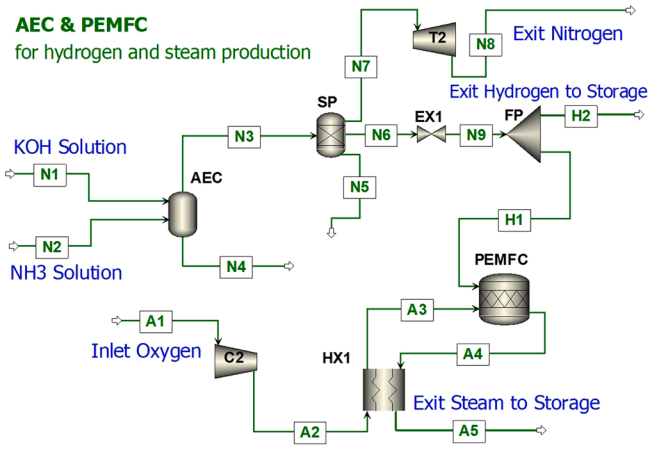

(b) Flowchart for AEC and PEMFC systems

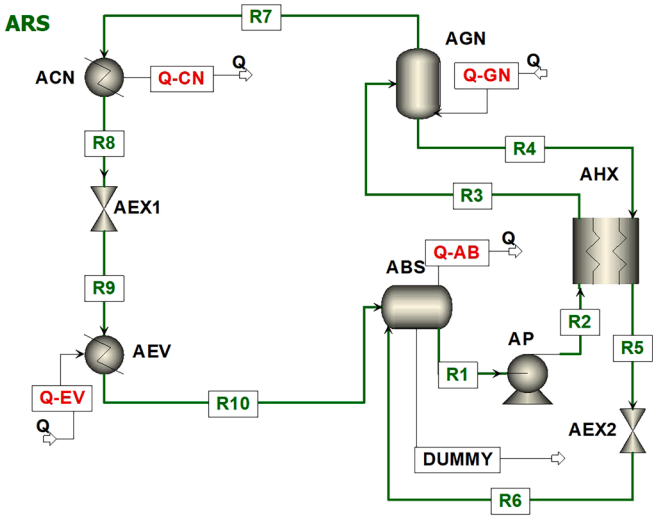

(c) Flowchart for ARS system

Fig. 2. Aspen flowcharts for the hybrid engine: (a) GT and SOFC, (b) onboard hydrogen production, and (c) ARS system.

transferred to the anode, while the electrons are transferred from the anode to the cathode. The resultant product of this reaction is high temperature steam and electric power. The specifications of the SOFC is listed in Table 1. The electrochemical reactions of the SOFC are listed below:.

- Anode: $H_2 + O^{2-} \rightarrow H_2O + 2e^-$
- Cathode: $0.5O_2 + 2e^- \leftrightarrow O^{2-}$
- Overall: $H_2 + 0.5O_2 \leftrightarrow H_2O$

The cell voltage, activation losses, ohmic losses, and concentration losses of the SOFC are summarized and expressed in Table 3.

The resultant power of the SOFC can be evaluated as follows:.

$$\dot{W}_{SOFC} = iA_t V_c \xi \tag{4}$$

where ξ is an inverter efficiency of 95%. The electric efficiency of the SOFC can be determined by Eqn. (5), while the thermal energetic and exergetic efficiencies can be evaluated by Eqn. (6). The SOFC added heat, $\dot{Q}_{SOFC}$, is estimated as the summation of the added heat through the

Table 1
Specification of gas turbine engine (data from [21]).

Specification	Values
Engine Module	CENTAUR 40
Company name	Solar Turbine - A Caterpillar Company
Output Power	3500 kW (4700 hp)
Heat rate	12,905 kJ/kWh
Exhaust flow	68,185 kg/h
Exhaust temperature	445 °C

Table 2
Technical data and details of fuel cells: SOFC, PEMFC, and AEC [23–25].

Parameters	Symbols	Units	SOFC	PEMFC	AEC
Cell temperature	T_c	K	1073	343	333
Cell pressure	P_c	kPa	200	200	1000
Current density	i	A/m^2	5000	7700	8000
Exchange current density	i_o	A/m^2	1000	2290	3287
Active cell area	A_c	m^2	0.64	0.3	0.3
# of cells per a stack	Nc	–	100	50	100
# of stacks	Ns	–	8	2	4
Total area	A_t	m^2	512	30	120
Anode thickness	δ_{an}	μm	20	125	—
Cathode thickness	δ_{ca}	μm	50	350	—
Electrolyte thickness	δ_{el}	μm	200	350	—
Interconnect thickness	δ_{in}	μm	20	30	—
Effective GDL thickness	δ_{GDL}	μm	—	500	—
Effective hydrogen (or water) diffusivity	D_{eff,H_2-H_2O}	m^2/s	0.0001	0.0000149	—
Effective oxygen & nitrogen diffusivity	D_{eff,O_2-N_2}	m^2/s	0.00002	—	—
Effective oxygen & water diffusivity	D_{eff,O_2-H_2O}	m^2/s	—	0.00000295	—
Water diffusivity in Nafion	D_λ	m^2/s	—	3.81E-10	—
Cathode Transfer Coefficient	α	–	0.5	0.3	
Porosity of anode	ε_{na}	–	0.5	0.5	0.5
Porosity of cathode	ε_{ca}	–	0.5	0.5	0.5
Porosity of GDL	ε_{GDL}	–	—	0.6	—
Tortuosity for anode and cathode	ξ	–	6	6	6
Fuller diffusion volume of hydrogen	ν_{H_2}	m^3	7.07	—	—
Fuller diffusion volume of water	ν_{H_2O}	m^3	12.7	—	—
Fuller diffusion volume of oxygen	ν_{O_2}	m^3	16.6	—	—
Fuller diffusion volume of nitrogen	ν_{N_2}	m^3	17.9	—	—

anode and cathode including the heat of the SR and WSG.

$$\eta_{SOFC,e} = \frac{V_c}{E_N} \text{ and } \eta_{SOFC,th} = \frac{\dot{W}_{SOFC}}{\dot{Q}_{SOFC}} \tag{5}$$

$$\psi_{SOFC,th} = \frac{\dot{W}_{SOFC}}{\dot{E}x^{Q}_{SOFC}} \tag{6}$$

3.2.2. Proton exchange membrane fuel cell (PEMFC)

The proton exchange membrane fuel cell (PEMFC) consists of a membrane electrode assembly (MEA), where each large side of a membrane has a gas diffusion layer (GDL), a bipolar plate, a current collector plate, and a compression plate. These plates formed one cell of PEM. Air and hydrogen are brought to the bipolar plates and flow into the channels of plates [29]. Then the gases are diffused by the GDL on either side of MEA, which is made of platinum. At contact of platinum of electrodes, the dihydrogen is split into protons H^+ and electrons, which are flowing through the GDL, bipolar, current collectors and the circuit, while the MEA is acting as a barrier to them. These electrons are combined with dioxygen at contact with platinum of the electrode to form O^{2-}. Then the H^+ is travelling through the MEA to combine with O^{2-} to form water, which is transferred out of the fuel cell with the air flow. The electrochemical reactions of PEMFC are the following:.

- Anode: $H_2 \rightarrow 2H^+ + 2e^-$
- Cathode: $0.5O_2 + 2H^+ + 2e^- \rightarrow H_2O$
- Overall: $H_2 + 0.5O_2 \rightarrow H_2O$

The cell voltage, activation losses, ohmic losses, and concentration losses of the PEMFC are summarized and given in Table 3 [28]. The gross power of PEMFC is expressed as:.

$$\dot{W}_{PEMFC} = iA_tV_c\xi \tag{7}$$

The electric efficiency of PEMFC is the ratio of cell voltage and Nernst voltage, and the thermal and exergetic efficiency is the ratio of electric power of PEMFC to the low heating value of hydrogen and exergetic flow rate of H1, respectively [30].

$$\eta_{PEMFC,e} = \frac{V_c}{E_N} \tag{8}$$

$$\eta_{PEMFC,th} = \frac{\dot{W}_{PEMFC}}{\dot{m}_{H1}LHV_{H_2}} \text{ and } \psi_{PEMFC,th} = \frac{\dot{W}_{PEMFC}}{\dot{E}x_{H1}} \tag{9}$$

3.2.3. Aluminum electrolysis cell (AEC)

This electrolysis cell decomposes ammonia into hydrogen and nitrogen gases by electrochemical reactions [31]. Two solutions are flowing into the cell: potassium hydroxide solution (5 M of KOH) to the cathode and ammonium solution (5 M of NH_3) to the anode at room temperature. KOH is strong alkali to make the water alkaline and produce hydroxide ions. At that moment, the ammonia in the anode side reacts with hydroxide ions to produce nitrogen gas, water, and free electrons. Therefore, the electrons pass through the electrolyte solution of alkalized water to electrochemically decompose water into hydrogen gas and OH^-. Hence, the nitrogen gas releases from the anode side and hydrogen gas releases from the cathode side. The electrochemical reaction is formed as follows:.

- Anode: $2NH_3 + 6OH^- \rightarrow N_2 + 6H_2O + 6e^-$
- Cathode: $6H_2O + 6e^- \rightarrow 3H_2 + 6OH^-$
- Overall: $2NH_3 \rightarrow 3H_2 + N_2$

The cell voltage is evaluated based on the experimental data done by [15] by evaluating the trendline equations of all activation, ohmic, and concentration losses to predict the cell voltage after verifying multiple experimental values of the cell voltage, based on the electrodes of the platinum carbon nanotubes (Pt-CNT) films. Therefore, the cell voltage can be defined as in Eqn. (10), and the Nernst voltage, activation loss, ohmic loss, and concentration loss are described by Eqns. (11–14).

$$V_c = E_N - \eta_{act} - \eta_\Omega - \eta_{con} \tag{10}$$

$$E_N = -\frac{\Delta\overline{g}}{3F} - \frac{\overline{R}T_c}{3F}\ln\left(\frac{1}{p^{0.5}_{N_2}p^{1.5}_{H_2}}\right) \tag{11}$$

$$\eta_{act} = \frac{2.3\overline{R}T_c}{3\alpha F}\ln\left(\frac{i}{i_o}\right) \tag{12}$$

$$\eta_\Omega = iRA_e \tag{13}$$

$$\eta_{con} = \left(1+\frac{1}{\beta}\right)\frac{\overline{R}T_c}{3F}\ln\left(\frac{i_L}{i_L - i}\right) \tag{14}$$

where i_o is the exchange current density, which is estimated as 1.16×10^{-8} mA/cm^2. α is the transfer coefficient, and it is calculated to

Table 3
Modelling the SOFC and PEMFC [26–28].

	SOFC	PEMFC
Cell voltage		
	$V_c = E_N - \eta_{act} - \eta_{\Omega} - \eta_{con}$	$V_c = E_N - \eta_{act} - \eta_{\Omega} - \eta_{con}$
Nernst Voltage	$E_N = -\frac{\Delta \bar{g}}{2F} - \frac{\bar{R}T_c}{2F}\ln\left(\frac{p_{H_2O}}{p_{H_2}\sqrt{p_{O_2}}}\right)$	$E_N = -\frac{\Delta \bar{g}}{2F} - \frac{\bar{R}T_c}{2F}\ln\left(\frac{p_{H_2O}}{p_{H_2}\sqrt{p_{O_2}}}\right)$
Activation polarization		
	$\eta_{act} = \eta_{act,an} + \eta_{act,ca}$	$\eta_{act} = \eta_{act,an} + \eta_{act,ca}$
By anode	$\eta_{act,an} = \frac{\bar{R}T_c}{2\alpha_{an}F}\sinh^{-1}\left(\frac{i}{2i_{0,an}}\right)$	$\eta_{act,an}$ = negligible
	Exchange current density of anode	
	$i_{0,an} = \gamma_{an}\left(\frac{P_{H_2}}{P_{ref}}\right)\left(\frac{P_{H_2O}}{P_{ref}}\right)\exp\left(-\frac{E_{act,an}}{\bar{R}T_c}\right)$	
	Pre-exponential coefficient for anode:	
	$\gamma_{an} = 7 \times 10^9$ A/m^2	
By cathode	$\eta_{act,ca} = \frac{\bar{R}T_c}{2\alpha_{ca}F}\sinh^{-1}\left(\frac{i}{2i_{0,ca}}\right)$	$\eta_{act,ca} = \frac{\bar{R}T_c}{2\alpha_{ca}F}\ln\left(\frac{i}{i_{0,ca}}\right)$
	Exchange current density of cathode	Exchange current density of cathode
	$i_{0,ca} = \gamma_{ca}\left(\frac{P_{O_2}}{P_{ref}}\right)^{0.25}\exp\left(-\frac{E_{act,ca}}{\bar{R}T_c}\right)$	$i_{o,ca} = i_{0,ref} \times \frac{C_{O_2,ca}}{C_{O_2,ref}}$
	Pre-exponential coefficient for cathode:	Concentration of oxygen:
	$\gamma_{ca} = 2 \times 10^9$ A/m^2	$C_{O_2,ref} = \frac{P_0 x_{O_2,ref}}{\bar{R}T_0}$ and $C_{O_2,ca} = \frac{P_c x_{O_2,ca}}{\bar{R}T_c}$
Ohmic loss		
Ohmic losses	$\eta_{\Omega} = i(\rho_{an}\delta_{an} + \rho_{ca}\delta_{ca} + \rho_{el}\delta_{el} + \rho_{in}\delta_{in})A_c$	$\eta_{\Omega} = \left(\frac{\delta_{mem}}{\kappa_{mem}} + \frac{\delta_{CCL}}{f_{CCL}^{1.5}\kappa_{CCL}}\right)i$
	Specific material resistivity:	Ionomer fraction:
	$\rho_{an} = 2.98 \times 10^{-5}\exp\left(-\frac{1392}{T_c}\right)$	$f_{CCL} = 0.15$
	$\rho_{ca} = 8.114 \times 10^{-5}\exp\left(\frac{600}{T_c}\right)$	Conductivity of Nafion:
	$\rho_{el} = 2.94 \times 10^{-5}\exp\left(\frac{10,350}{T_c}\right)$	$\kappa = (0.005139\lambda - 0.00326) \times \exp\left(1268\left(\frac{1}{303} - \frac{1}{T_c}\right)\right)$
	$\rho_{in} = 1.257 \times 10^{-5}\exp\left(\frac{4690}{T_c}\right)$	
Concentration losses		
	$\eta_{con} = \eta_{con,an} + \eta_{con,ca}$	$\eta_{con} = \eta_{con,an} + \eta_{con,ca}$
By anode	$\eta_{con,an} = -\frac{\bar{R}T_c}{2F}\ln\left(1 - \frac{i}{i_{L,an}}\right) + \frac{\bar{R}T}{2F}\ln\left(1 + \frac{P_{H_2}i}{P_{H_2O}i_{L,an}}\right)$	$\eta_{con,an}$ = negligible
	Limiting current density of anode:	
	$i_{L,an} = \frac{2FP_{H_2}D_{an(eff)}}{\bar{R}T_c}$	
By cathode	$\eta_{con,ca} = -\frac{\bar{R}T_c}{2F}\ln\left(1 - \frac{i}{i_{L,ca}}\right)$	$\eta_{con,ca} = \left(1 + \frac{1}{\alpha_{ca}}\right)\frac{\bar{R}T_c}{4F}\ln\left(\frac{i_L}{i_{L,ca} - i}\right)$
	Limiting current density of cathode:	Limiting current density of cathode:
	$i_{L,ca} = \frac{2FP_{O_2}D_{ca(eff)}}{\bar{R}T_c}$	$i_{L,ca} = i_{L,ref} \times \frac{C_{O_2,ca}}{C_{O_2,ref}} \times \frac{D_{O_2,ca}}{D_{O_2,ref}}$
Effective diffusivity	Ordinary diffusion coefficient	Effective diffusion coefficient:
	$D_{O,ik} = \frac{1 \times 10^{-7}T^{1.25}\left(M_i^{-1} + M_k^{-1}\right)^{0.5}}{P\left(\nu_i^{1/3} + \nu_k^{1/3}\right)}$	$D_{O_2,eff} = D_{O_2,N_2}\big\vert_{(T_c,P_c)}\varepsilon^{3.6}(1 - S_{av})^3$
	Effective ordinary diffusion coefficient:	Reference diffusion coefficient:
	$D_{O,i(eff)} = D_{O,i}\left(\frac{\varepsilon}{\xi}\right)$	$D_{O_2,ref} = D_{O_2,N_2}\big\vert_{(T_0,P_0)}\varepsilon^{3.6}$
	Knudsen diffusion coefficient:	Liquid water saturation:
	$D_{K,i} = 97r\sqrt{\frac{T}{M_i}}$	$S_{av} = 0.1$
	Effective Knudsen diffusion coefficient:	Binary diffusion coefficient [26]:
	$D_{K,i(eff)} = D_{K,i}\left(\frac{\varepsilon}{\xi}\right)$	$D_{ij}\big\vert_{(T,P)} = \frac{a}{P}\left(\frac{T}{\sqrt{T_{cr,i}T_{cr,j}}}\right)^b \times \left(P_{cr,i}P_{cr,j}\right)^{\frac{1}{3}} \times \left(T_{cr,i}T_{cr,j}\right)^{\frac{5}{12}} \times \left(\frac{1}{M_i} + \frac{1}{M_j}\right)^{\frac{1}{2}}$
	Overall diffusion coefficient:	
	$\frac{1}{D_{i(eff)}} = \frac{1}{D_{K,i(eff)}} + \frac{1}{D_{O,i(eff)}}$	
	Effective diffusivity of anode and cathode:	
	$D_{an(eff)} = \left(\frac{P_{H_2O}}{P_{an}}\right)D_{H_2(eff)} + \left(\frac{P_{H_2}}{P_{an}}\right)D_{H_2O(eff)}$	
	$D_{ca(eff)} = D_{O_2(eff)}$	$a = 2.75 \times 10^{-4}$ and $b = 1.823$

be 0.85, and β is a function of the transfer coefficient and equals to$k\alpha$, where k is a constant of 0.0218. The limiting current density i_L equals to 1.35 A/cm^2. A_e is the electrode surface area which is equal to 1.75 cm^2, and R is the resistance of Pt-CNT electrode, which is measured to be 0.701 Ω [15]. The required power of AEC is defined as:

$$\dot{W}_{AEC} = iA_tV_c\xi \tag{15}$$

The electric efficiency of AEC is the ratio of Nernst voltage to cell voltage since it requires more voltage to operate the cell. The thermal and exergetic efficiency is the ratio of the hydrogen energy produced by

the cell and exergetic flow rate of N9 divided by the amount required power to operate this cell.

$$\eta_{AEC,e} = \frac{E_N}{V_c} \tag{16}$$

$$\eta_{AEC,th} = \frac{\dot{m}_{N9} LHV_{H_2}}{\dot{W}_{AEC}} \text{ and } \psi_{AEC,th} = \frac{\dot{E}x_{N9}}{\dot{W}_{AEC}} \tag{17}$$

The AEC-PEMFC system is used for hydrogen production, which is operated separately from the engine, as shown in Fig. 2-b. However, the amount of the required power ($\dot{W}_S$) is fed by the overall engine power. The performance of this storage system, η_S andψ_S, can be estimated as follows:

$$\dot{W}_S = \dot{W}_{T2} - \dot{W}_{C2} + \dot{W}_{PEMFC} - \dot{W}_{AEC} \tag{18}$$

$$\eta_S = \frac{\dot{E}_{out,S}}{\dot{E}_{in,S}} = \frac{\dot{W}_S + \dot{m}_{H_2} LHV_{H_2}}{\dot{m}_{A1} h_{A1} + \dot{m}_{N1} h_{N1} + \dot{m}_{N2} h_{N2} - \dot{m}_{N5} h_{N5}} \tag{19}$$

$$\psi_S = \frac{\dot{E}x_{out,S}}{\dot{E}x_{in,S}} = \frac{\dot{W}_S + \dot{E}x_{H_2}}{\dot{E}x_{A1} + \dot{E}x_{N1} + \dot{E}x_{N2} - \dot{E}x_{N5}} \tag{20}$$

3.3. Modeling of energy recovery system

The energy recovery system consists of two subsystems: thermoelectric generator (TG) and absorption refrigeration system (ARS). The TG is a device that converts excessive waste heating load into electrical power. It is based on a thermoelectric module, which comprises p- and n-type semiconductors connected in series or parallel. The principle of electricity generation of the TG is governed by the Seebeck effect. The amount of heat transferred from the exhaust to the TG is expressed as$\dot{Q}_{TG}$, and the hot and cold junction heat transferred is defined as $\dot{Q}_{H,TG}$ and$\dot{Q}_{L,TG}$, respectively. The resultant power of the TG is defined as$\dot{W}_{TG}$, while the performance of the TG can be measured by electric efficiency ($\eta_{e,TG}$), thermal efficiency ($\eta_{th,GT}$), and exergetic efficiency (ψ_{TG}), as defined below [32].

$$\dot{Q}_{TG} = \dot{m}_{B7}(h_{B7} - h_{B8}) \tag{21}$$

$$\dot{Q}_{H,TG} = N\left(\beta I T_H - \frac{I^2 r}{2} + K(T_H - T_L)\right) \tag{22}$$

$$\dot{Q}_{L,TG} = N\left(\beta I T_L + \frac{I^2 r}{2} + K(T_H - T_L)\right) \tag{23}$$

$$\dot{W}_{TG} = \dot{Q}_{H,TG} - \dot{Q}_{L,TG} \tag{24}$$

$$\eta_{e,TG} = \frac{\dot{W}_{TG}}{\dot{Q}_{H,TG}} \text{ and } \eta_{th,GT} = \frac{\dot{W}_{TG}}{\dot{Q}_{TG}} \tag{25}$$

$$\psi_{TG} = \frac{\dot{W}_{TG}}{\dot{E}x^{Q}_{TG}} \tag{26}$$

where β is the Seebeck coefficient, N is the number of thermoelectric units (1 0 0), I is the thermoelectric current, the current density of the TG (i) is 3000 A/m^2, and the active area of the TG (A_t) is 33.6 m^2 [33]. T_H is the hot junction temperature, which is the average temperature of B7 and B8, and T_L is the cold junction temperature, which is the ambient temperature, r is electric resistance, K is thermal conductance. Thermoelectric properties are function of temperature and can be expressed by the following [34]:

$$\beta = 2\left(2224 + 930.6T_m - 0.9905T_m^2\right) \times 10^{-9} \tag{27}$$

$$\rho_P = \rho_N = \left(5112 + 163.4T_m - 0.6279T_m^2\right) \times 10^{-9} \tag{28}$$

$$\lambda_P = \lambda_N = \left(62605 - 277.7T_m + 0.413T_m^2\right) \times 10^{-9} \tag{29}$$

$$T_m = \frac{T_H + T_L}{2} \tag{30}$$

$$r = \frac{\rho_P + \rho_N}{C} \tag{31}$$

$$K = \frac{\lambda_P + \lambda_N}{C} \tag{32}$$

where ρ is the electrical resistivity, λ is the heat transfer coefficient, C is the geometry factor and equals to 0.5 m, and T_m is the mean temperature [35].

The ARS uses ammonia-water refrigerant and consists of a generator (AGN), absorber (ABS), two expansion valves (AEX1 and AEX2), evaporator (AEV), a pump (AP), and condenser (ACN). Table 4 displays the partial mass balance and energy balance equations. In the ARS systems, three solutions are considered: pure ammonia solution (y_{pure}), weak ammonia solution (y_{ws}) and strong ammonia solution (y_{ss}) [36,37]. The performance of the ARS is measured based on the energetic and exergetic COP of the cycle as written below:

$$COP_{en} = \frac{\dot{Q}_{AEV}}{\dot{Q}_{AGN} + \dot{W}_{AP}} \text{ and } COP_{ex} = \frac{\dot{E}x^{Q}_{AEV}}{\dot{E}x^{Q}_{AGN} + \dot{W}_{AP}} \tag{33}$$

3.4. Fuel blends and its combustion

The sustainable fuels are chosen to be hydrogen (H_2), methanol (CH_3OH), and ethanol (CH_3OHCH_2) and dimethyl-ether (DME) (CH_3OCH_3) because they are ecofriendly and have high ignition temperature with less or moderate ignition energy, and they can blend together [38–40] and utilized in transportation engines to generate electrical power [41–44]. The fuel properties are presented in [20]. Table 5 provides the chemical reactions of fuel blends (RF1 to RF5) that occurred in the designed system. Five fuel blends are formed, where hydrogen is the base, and their mass ratio are listed. The chemical reactions of the steam reformer (SR), water gas shift (WGS), afterburner (BR), and combustion chamber of the engine (CC) are also introduced in the same table.

3.5. Overall performance of locomotive engine

The engine power ($\dot{W}_{eng}$) and heat required ($\dot{Q}_{eng}$) are given in Eqns. (34 and 35). The power and heat exergy rates are defined by $\dot{E}x^{W}_{eng}$ and$\dot{E}x^{Q}_{eng}$, respectively. The overall performance of the hybrid locomotive engine can be measured using the thermal efficiency (η_{eng}) and exergetic efficiency (ψ_{eng}) of the engine, which are explained in Eqns. (38 and 39).

$$\dot{W}_{eng} = \dot{W}_{GT} + \dot{W}_{TG} + \dot{W}_{SOFC} + \dot{W}_S - \dot{W}_{AP} \tag{34}$$

Table 4
Partial mass balance and energy balance equations of the ARS.

Comp#	Partial Mass Balance	Energy Balance
ACN	$y_{NH_3,R7} = y_{NH_3,R8} = y_{pure}$	$\dot{Q}_{ACN} = \dot{m}_{R8}(h_{R7} - h_{R8})$
AEV	$y_{NH_3,R7} = y_{NH_3,R8} = y_{pure}$	$\dot{Q}_{AEV} = \dot{m}_{R9}(h_{R9} - h_{R10})$
AGN	$\dot{m}_{R3} y_{NH_3,R3} = \dot{m}_{R4} y_{NH_3,R4} + \dot{m}_{R7} y_{NH_3,R7}$	$\dot{Q}_{AGN} = \dot{m}_{R7} h_{R7} + \dot{m}_{R4} h_{R4} - \dot{m}_{R3} h_{R3}$
AHX	$y_{NH_3,R2} = y_{NH_3,R3} = y_{ss} y_{NH_3,R4} = y_{NH_3,R5} = y_{ws}$	$\dot{Q}_{AHX} = \dot{m}_{R4}(h_{R4} - h_{R5})$
ABS	$\dot{m}_{R6} y_{NH_3,R6} + \dot{m}_{R10} y_{NH_3,R10} = \dot{m}_{R1} y_{NH_3,R1}$	$\dot{Q}_{ABS} = \dot{m}_{R6} h_{R6} + \dot{m}_{R10} h_{R10} - \dot{m}_{R1} h_{R1}$
AP	$y_{NH_3,R1} = y_{NH_3,R2} = y_{ss}$	$\dot{W}_{AP} = \dot{m}_{R1}(h_{R2} - h_{R1})$

$$\dot{Q}_{eng} = \dot{Q}_{CC} + \dot{Q}_{BR} \tag{35}$$

$$\dot{E}x^{W}_{eng} = \dot{W}_{eng} \tag{36}$$

$$\dot{E}x^{Q}_{eng} = \dot{E}x^{Q}_{CC} + \dot{E}x^{Q}_{BR} \tag{37}$$

$$\eta_{eng} = \frac{\dot{E}_{out,eng}}{\dot{E}_{in,eng}} = \frac{\dot{W}_{eng} + \dot{Q}_{AEV}}{\dot{Q}_{eng}} \tag{38}$$

$$\psi_{eng} = \frac{\dot{E}x_{out,eng}}{\dot{E}x_{in,eng}} = \frac{\dot{E}x^{W}_{eng} + \dot{E}x^{Q}_{AEV}}{\dot{E}x^{Q}_{eng}} \tag{39}$$

4. Results and discussion

This section presents the results and discussion of the thermodynamic analysis and parametric studies of the hybrid locomotive engine as written in the subsections below.

4.1. Thermodynamic analysis Results

The hybrid locomotive engine was modelled using Aspen Plus by selecting two equations of state, the Soave-Redlich-Kwong (SRK) for the hydrocarbons and the electrolyte property method (ELECNRTL) for modelling the AEC [45]. The modeling to the locomotive model is validated through previous research by performing Aspen PLUS simulation to a traditional engine with its operating conditions, and the error between the actual and simulation was obtained to be 3% to 7% for temperature, pressure, and power values as reported in [20]. The first step is to evaluate the thermodynamic data, including the mass flow rate, temperature, pressure, specific enthalpy, specific entropy, specific physical and chemical exergy, and total exergy rate for each stream. According to the flowcharts of the hybrid engine in Fig. 2 using the fuel blend RF1 (methane and hydrogen), Table 6 presents the thermodynamic data of the GT engine and SOFC system, including streams B1 to B9, M1 to M5, and fuels F1, F2, and W1 as shown in Fig. 2-a. Also, the thermodynamic data are estimated for the AEC and PEMFC systems in Table 7, consisting of streams N1 to N9 for the hydrogen and nitrogen production, A1 to A5 for electricity generation, and H1 and H2 for hydrogen production. In addition, Table 8 shows the thermodynamic data for streams R1 to R10, including mass fraction of ammonia and water, and the quality of the mixed refrigerant, to provide cooling load for the train.

Table 9 displays the performance of the system components by evaluating the amount of required and rejected heat, the amount of required and generated power, exergy destruction rate, and thermal and electric efficiency and exergetic efficiency. As shown in the table, the rejected heat varies from 8 kW to 160 kW for the SR and WGS reactors to 290 to 1020 kW for the fuel cells. Also, the required heat records a similar amount of 7600 kW for combustion in CC and BR. Likewise, the required power was estimated to be less than 20 kW for AP and C2, and 450 kW for AEC, and 7900 kW for C, while the generated power was obtained to be about 11300 kW for T1, 300 W for T2, 225, 2740, and 960 kW for the PEMFC, SOFC, and TG, respectively. The fuel cells have electric efficiency of more than 75%, and thermal efficiency ranging from 30 to 75%. The minimum thermal efficiency was calculated for SOFC to be 33%, while the minimum exergetic efficiency was estimated to be 2% for the AEV.

The performance of the subsystems and overall systems are illustrated in Table 10. The performance of the GT engine only using RF1 is 22.3% energetic efficiency and 32% exergetic efficiency. If this GT engine is operated using diesel oil, the diesel GT can accomplish an overall efficiency of 33.5% and a net power of 3639 kW and combustion heat of 10870 kW, which is higher than the GT only using RF1. The SOFC system can attain 34 % and 43% of thermal and exergetic efficiencies, respectively. The energy recovery system consisting of the TG and ARS can produce about 940 kW net work and 615 kW of cooling load by converting the net exhaust heat of 5620 kW into electricity and cooling load with 28% efficiency. The hydrogen production can fulfill about 40% overall efficiency by generating electricity of 225.3 kW using the PEMFC and producing hydrogen of 367.8 kW (0.003 kg/s H_2). Therefore, the resultant performance is increased to about 48% thermal efficiency and 51% exergetic efficiency. The total electricity generated by using all these systems is 6844.3 kW without hydrogen flow rate. If we consider only the electric generation, then the overall performance will be 46% thermal efficiency and 48% exergetic efficiency.

4.2. Parametric studies

Several parameters were selected to be examined to understand the behavior of the designed system, starting with the effect of different fuel blends, splitting ratio of SP1, mass flowrates of AEC, current density of fuel cells, and finally constant active area and current density of fuel cells.

4.2.1. The effect of fuel blends

Five fuel blends are considered in this paper, which are RF1 to RF5,

Table 5
The chemical reactions of fuel blends in the engine.

Fuels	Mass ratio	SR	WGS	CC and BR
RF1	75% CH_4, 25% H_2	$CH_4 + H_2O \rightarrow CO + 3H_2$	$CO + H_2O \rightarrow CO_2 + H_2$	$CH_4 + 2O_2 \rightarrow CO_2 + 2H_2O$ $2H_2 + O_2 \rightarrow 2H_2O$ $2CO + O_2 \rightarrow 2CO_2$
RF2	75% CH_3OH, 25% H_2	$CH_3OH \rightarrow CO + 2H_2$	$CO + H_2O \rightarrow CO_2 + H_2$	$CH_3OH + 1.5O_2 \rightarrow CO_2 + 2H_2O$ $2H_2 + O_2 \rightarrow 2H_2O$ $2CO + O_2 \rightarrow 2CO_2$
RF3	60% CH_3OHCH_2, 40% H_2	$CH_3OHCH_2 \rightarrow CH_4 + CO + H_2$ $CH_4 + H_2O \rightarrow CO + 3H_2$	$CO + H_2O \rightarrow CO_2 + H_2$	$CH_3OHCH_2 + 3O_2 \rightarrow 2CO_2 + 3H_2O$ $2H_2 + O_2 \rightarrow 2H_2O$ $2CO + O_2 \rightarrow 2CO_2$
RF4	60% CH_3OCH_3, 40% H_2	$CH_3OCH_3 \rightarrow CH_4 + CO + H_2$ $CH_4 + H_2O \rightarrow CO + 3H_2$	$CO + H_2O \rightarrow CO_2 + H_2$	$CH_3OCH_3 + 3O_2 \rightarrow 2CO_2 + 3H_2O$ $2H_2 + O_2 \rightarrow 2H_2O$ $2CO + O_2 \rightarrow 2CO_2$
RF5	15% CH_4, 15% CH_3OH, 15% CH_3OHCH_2, 15% CH_3OCH_3, 40% H_2	$CH_4 + H_2O \rightarrow CO + 3H_2$ $CH_3OH \rightarrow CO + 2H_2$ $CH_3OHCH_2 \rightarrow CH_4 + CO + H_2$ $CH_3OCH_3 \rightarrow CH_4 + CO + H_2$	$CO + H_2O \rightarrow CO_2 + H_2$	$CH_4 + 2O_2 \rightarrow CO_2 + 2\,H_2O$ $CH_3OH + 1.5O_2 \rightarrow CO_2 + 2H_2O$ $CH_3OHCH_2 + 3O_2 \rightarrow 2CO_2 + 3H_2O$ $CH_3OCH_3 + 3O_2 \rightarrow 2CO_2 + 3H_2O$ $2H_2 + O_2 \rightarrow 2H_2O$ $2CO + O_2 \rightarrow 2CO_2$

Table 6
Results of thermodynamic data for Fig. 2-a.

#	$\dot{m}$ [kg/s]	T [K]	P [kPa]	h [kJ/kg]	s [kJ/(kg.K)]	ex_{ph} [kJ/kg]	ex_{ch} [kJ/kg]	$\dot{E}x$ [kW]
B1	14.0	298.2	100	−0.2	0.1431	−1.1	4.6	49.0
B2	14.0	780.1	2000	508.0	0.2818	465.7	4.6	6585.0
B3	14.6	1873.2	2000	−171.5	1.3924	1727.5	573.0	33540.7
B4	14.6	1274.6	200	−1031.8	1.5722	813.6	573.0	20216.5
B5	10.2	1274.6	200	−1031.8	1.5722	813.6	573.0	14151.5
B6	4.4	1274.6	200	−1031.8	1.5722	813.6	573.0	6064.9
B7	14.6	923.2	200	−2116.4	1.0043	476.5	72.0	8013.4
B8	14.6	823.2	200	−2247.9	0.8536	390.0	72.0	6749.3
B9	14.6	623.2	200	−2501.2	0.5015	241.7	72.0	4582.6
F1	0.58	293.2	1000	−3529.9	−6.2855	970.7	67889.1	39938.7
F2	0.01	298.2	200	−3502.1	−3.9026	289.0	67889.1	681.8
M1	0.03	290.3	100	−11862.6	−6.9973	−5.6	22825.2	684.6
M2	0.03	473.2	200	−6588.6	2.0035	463.4	24793.9	757.7
M3	0.03	673.2	200	−6313.7	2.7357	749.9	24474.5	756.7
M4	10.24	923.2	200	−1839.7	1.0315	471.9	365.9	8568.6
M5	14.61	1030.5	200	−1597.8	1.2125	569.0	426.8	14549.0
W1	0.02	298.2	100	−16042.9	−9.0569	−0.01	527.3	10.5

Table 7
Results of thermodynamic data for Fig. 2-b.

#	$\dot{m}$ [kg/s]	T [K]	P [kPa]	h [kJ/kg]	s [kJ/(kg.K)]	ex_{ph} [kJ/kg]	ex_{ch} [kJ/kg]	$\dot{E}x$ [kW]
A1	0.020	298.2	100	−0.26	0.0027	−1.1	123.0	2.5
A2	0.020	472.6	400	163.6	0.0747	141.5	265.6	5.3
A3	0.020	422.6	400	115.7	−0.0327	125.5	249.6	5.0
A4	0.022	353.2	200	−12973.6	−6.7661	32.3	451.6	9.9
A5	0.022	369.4	200	−12930.1	−6.3861	101.7	520.4	11.5
H1	0.002	429.6	200	1873.1	2.3932	1158.9	118274.0	243.5
H2	0.003	429.6	200	1873.1	2.3932	1158.9	118274.0	365.2
N1	0.501	298.2	100	−14393.8	−7.7358	−2.1	1547.0	774.4
N2	0.500	293.2	1000	−13727.0	−9.5834	−75.6	4101.4	2050.7
N3	0.159	429.2	1000	−7469.0	−3.6690	553.6	13397.5	2132.1
N4	0.841	429.2	1000	−14095.2	−7.6475	213.4	1748.5	1471.2
N5	0.150	429.2	1000	−8121.0	−4.3920	516.8	10250.3	1535.4
N6	0.005	429.2	1000	1873.1	−4.2607	3142.6	120257.7	618.9
N7	0.004	429.2	1000	135.8	−0.3021	225.9	251.6	1.1
N8	0.004	350.0	400	53.5	−0.2424	125.7	151.4	0.7
N9	0.005	429.6	200	1873.1	2.3932	1158.9	118274.0	608.7

Table 8
Results of thermodynamic data for Fig. 2-c.

#	$\dot{m}$ [kg/s]	T [K]	P [kPa]	h [kJ/kg]	s [kJ/(kg.K)]	ex_{ph} [kJ/kg]	$\dot{E}x$ [kW]	y_{NH_3} [-]	y_{H_2O} [-]	Q [-]
R1	5	283.2	100	−9903	−10.5	44.5	222	0.524	0.476	0
R2	5	283.5	2000	−9900	−10.5	47.1	235	0.524	0.476	0
R3	5	345.5	2000	−9608	−9.6	61.7	309	0.524	0.476	0
R4	3.32	398.2	2000	−11747	−8.5	71.6	237	0.324	0.676	0
R5	3.32	306.1	2000	−12188	−9.8	5.4	18	0.324	0.676	0
R6	3.32	292.3	100	−12188	−9.8	0.8	3	0.324	0.676	0.04
R7	1.68	398.2	2000	−3403	−6.3	448.4	755	0.919	0.081	1
R8	1.68	333.2	2000	−4125	−8.3	322.9	543	0.919	0.081	0.61
R9	1.68	252.8	100	−4125	−7.3	31.9	54	0.919	0.081	0.77
R10	1.68	301.2	100	−3760	−6.0	1.6	3	0.919	0.081	0.92

as well as diesel (as the base fuel). Table 11 displays the mass flowrates of intake air to the GT, intake fuels in streams F1 and F2, and steam in stream W1. These number are considered in that way to fulfill a net power of the GT engine to be greater than or equal to 3355 kW, which is the power of the EMD 16-710G3 [9] that is capable of operating a train. As shown in this table, all the sustainable fuel blends have higher HHV and LHV compared to diesel fuel, reflecting on lower mass flowrates of these fuels than the diesel fuels.

In the comparison of fuel blends, Fig. 3 presents the effect of these fuels on engine performance. From Fig. 3-a, the highest heat is needed for RF1 at 16.3 MW, followed by RF3 (14.6 MW), RF2 (14.2 MW), RF5 (14.1 MW), and the minimum heat is for RF4 (13.4 MW). This trend is different in the overall engine power, where the highest power is gained by RF5 (7.9 MW) and the lowest power is obtained by RF1 (6.8 MW). The cooling load remained constant at 915 kW. Fig. 3-b illustrates the values of generated power using the three subsystems of GT, SOFC, and TG. The TG provides an average electricity of 925 kW, while the power generated by others change to an average of 3500 kW, while the SOFC generates lower than this value in RF1 to RF3, with an average of 3020 kW, and higher than 3500 kW using RF4 and RF5 with an average of 3750 kW. The reason for this variation is the amount of hydrogen produced in the reactors and combustors to be utilized in the SOFC unit. This behavior accomplishes higher efficiencies using RF4 and RF5 above 60%, while the minimum efficiencies are obtained by RF1 (below 50%), as shown in Fig. 3-c. The equivalence ratio of the fuels considered in this study is about 0.95 that means the stoichiometric air–fuel ratio is less

Table 9
Results of the performance of components in the hybrid engine.

Comp. #	$\dot{Q}$ [kW]	$\dot{W}$ [kW]	$\dot{E}x_D$ [kW]	η_{th} [%]	η_e [%]	ψ [%]
C1	0.0	7905.4	1369.4	72.0	0	82.7
T1	0.0	11288.4	2035.9	72.0	0	84.7
C2	0.0	3.6	0.8	72.0	0	78.2
T2	0.0	0.3	0.1	72.0	0	74.0
AEC	1019.7	446.9	1133.5	49.8	79.5	35.7
PEMFC	292.4	225.3	13.2	77.1	77.7	76.6
SOFC	8111.5	2739.7	3600.0	33.8	86.9	43.2
CC	7564.7	0.0	19344.2	49.4	0.0	58.4
BR	7576.7	0.0	10758.1	49.4	0.0	26.1
SR	158.2	0.0	14.6	55.5	0.0	97.9
WGS	8.2	0.0	5.6	95.8	0.0	99.3
TG	1921.1	960.6	303.5	50.0	0.0	76.0
ACN	1215.0	0.0	83.5	100.0	0.0	88.9
AEV	615.1	0.0	132.8	100.0	0.0	2.0
AHX	1462.5	0.0	146.4	100.0	0.0	69.0
AGN	3346.0	0.0	157.4	100.0	0.0	81.3
ABS	2763.0	0.0	170.0	100.0	0.0	21.7
AP	0.0	17.3	4.1	70.0	0.0	76.0

Table 10
Performance of the major systems/components.

Major Systems/ Components	$\dot{W}_{net}$ [kW]	$\dot{Q}_{add}$ [kW]	$\dot{Q}_{cooling}$ [kW]	η_{th} [%]	ψ [%]
GT Engine					
GT	3383.0	15141.5	0	22.3	32.0
SOFC System					
SOFC	2739.7	0	0	33.8	43.2
SR	0	158.2	0	90.0	97.9
WGS	0	8.2	0	90.0	99.3
Energy Recovery					
TG	960.6	0	0	77.1	76.6
ARS	17.3	0	615.1	18.3*	9.5**
Hydrogen Production					
PEMFC	225.3	0	0	77.7	94.7
AEC	446.9 + 367.8 (H_2)	1019.7	0	30.4	35.7
Resultant Performance	7211.8	16327.6	615.1	47.94	50.98

* COP_{en}.
** COP_{ex}.

Table 11
Fuel and air mass flowrates with respect to fuels.

Parameters	Diesel	RF1	RF2	RF3	RF4	RF5
$\dot{m}_{B1}$ [kg/s]	15.00	14.00	13.00	13.00	13.00	13.00
$\dot{m}_{F1}$ [kg/s]	1.00	0.58	0.85	0.60	0.56	0.56
$\dot{m}_{F2}$ [kg/s]	0	0.01	0.01	0.01	0.01	0.01
$\dot{m}_{W1}$ [kg/s]	0	0.02	0.01	0.01	0.01	0.01
HHV [MJ/kg]	45.6	77.10	52.50	74.58	75.76	77.70
LHV [MJ/kg]	43.3	67.25	43.33	64.92	64.92	66.15

than the actual air–fuel ratio. The excess air is used for the SOFC system and afterburner BR. The combustion heat of RF1 is higher than others that is because it is proportional to the ignition temperature of methane (537°C) but higher than that of methanol (470°C), ethanol (365°C), and dimethyl ether (350°C). The minimum ignition energy of methane and hydrogen decreases by 30% by increasing the amount of hydrogen blend by 25% [46,47], and it is higher than that of others [48]. The produced work and added heat by a fuel is minimum for RF1 because the power varies inversely with the specific heat ratio (γ) of fuels, and the γ_{CH_4} is 1.32 and is the highest value [49].

The power required for the compressors is constant for all fuel types because they have same operating conditions and same mass flow rate of air. However, the generated power of turbines varies according to the fuel type. The highest turbine power is generated by using RF1 (11.3 MW) compared to other fuels as 11 MW for RF2, 10.9 MW for RF3, 10.8 MW for RF4, and 10.8 MW for RF5. Nevertheless, the fuel RF1 produces the lowest SOFC power due to the chemical properties of methane and combustion characteristics of methane. Therefore, the high combustion heat and low resultant power of methane-hydrogen blend decrease the overall thermal efficiency of the entire engine by using RF1.

A detailed discussion about the systems is presented focusing on different heating loads, reactor loads, generated and produced power to comprehend the system behavior with respect to fuels blends. As shown in Fig. 4-a, the heating loads of the CC and BR are bar-graphed with an average of 7.2 MW for CC and 6.3 MW for BR; the maximum and minimum values are obtained by RF3 and RF4 for CC and RF1 and RF4 for BR, respectively. The cooling load has maintained its value of 915 kW. Additionally, the reforming reactors (SR) have higher heating loads above 40 kW with a maximum value of 158 kW for RF1 and a minimum value of 40 kW for RF4, while WGS reactors produce heat with an average of 10 kW, as shown in Fig. 4-b.

The performance of the SOFC has been impacted using fuel blends as graphed in Fig. 5. The generated power from the SOFC is estimated to be with an average of 3000 kW, but their exhaust heat is higher than 8000 kW. The design of the SOFC can be executed using two methods: the inner specifications and the moles of required hydrogen, which affect the SOFC size or number of stacks. As shown in Fig. 5-a, the number of stacks is 11 units for RF4 and RF5, and dropped to 10 stacks, and again to 8 for RF1. Therefore, the moles of the required hydrogen in the SOFC can be the minimum value of 13 mol/s for RF1 followed by RF3, and the maximum of 18 mol/s for RF4 and RF5, as presented in Fig. 5-b. The electric efficiency is held constant about 87%, while the thermal and exergetic efficiency have the same trend as the highest performance using RF4 and lowest performance using RF3.

The environmental impact can be compared between this hybrid locomotive engine and the traditional GT using diesel fuel as presented in Table 12. The mass flow rate of diesel at the B4 is 0.2 kg/s due to 80% of fuel utilization. The net power of the GT using diesel is 3639 kW, and the added heat of the CC is 10870 kW yielding the thermal efficiency to be 33.48%. Therefore, the CO_2 emission from the traditional GT can be 2.51 kg/s and can be increased to 2.82 kg/s if fuel combustion reaches 100%. The proposed hybrid engine can reduce emissions by about 50% using RF1, 65% using RF2, and more than 70% using RF3 to RF5.

4.2.2. Effect of splitting ratio

As shown in Fig. 2-a, the splitter SP1 is used to distribute the exit flow B4 to B5 utilized by SOFC system and B6 used by BR. This helps to estimate how much power is generated by the SOFC and its performance. Also, how many SOFC stacks are needed in designing the space of locomotive cabinet can be determined. As shown in Fig. 6, the mass flow rate ratios change from 0 as no flow passes through to B5 to 1 as all the flow passes through B5. Accordingly, the power and heat rejected from the SOFC increases from 0 to about 4.8 MW electric power and from 0 to 12 MW heat of SOFC. On the contrary, the heat of BR is decreased from 15 MW to 5 MW, as shown in Fig. 6-a. The electric efficiency is constantly obtained to be 87%, but the thermal and exergetic efficiency are declining from 60% to 35% and from 85% to 50%, respectively. Obviously, more output electricity should require a high number of stacks (from 2 to 11 stacks) at the same current density and same active area of 0.64 m^2, as shown in Fig. 6-b. The resultant engine power rises from 4 MW to 8 MW, which boosts the energetic and exergetic efficiency from 20 to 65% and 35% to 90%, respectively, as shown in Fig. 6-c.

4.2.3. Effect of mass flow rates of AEC

The hydrogen production system is useful to produce hydrogen fuel for the locomotive engine. it can be placed inside the locomotive cabinet or the second cabinet to be stored in tanks. However, the size of the AEC depends on the amount of hydrogen produced. Three parameters are

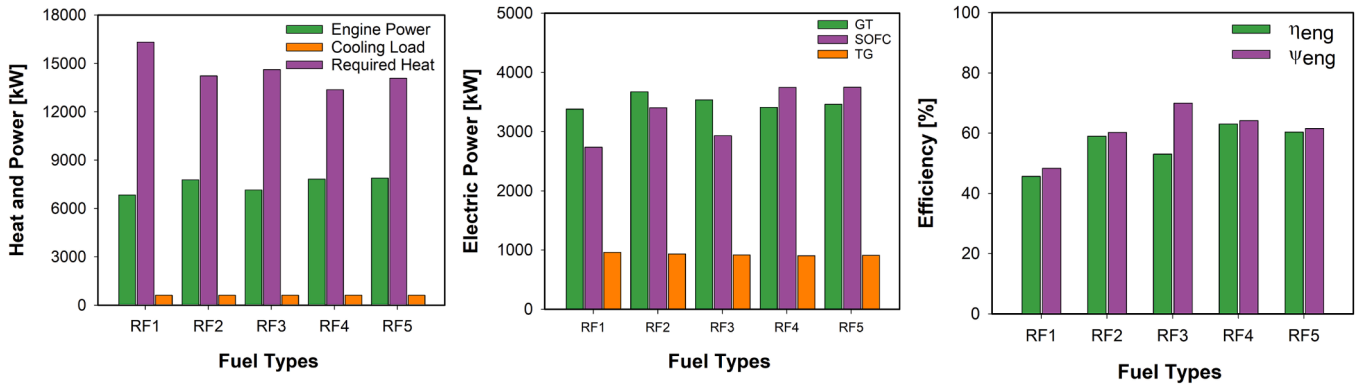

(a) Power and heat (b) Electric power (c) Overall efficiencies

Fig. 3. Comparative performance evaluation of the hybrid engine with various alternative fuels: (a) heat and power values of major components, (b) electric power of major components, and (c) overall energetic and exergetic efficiencyies of the hybrid engine.

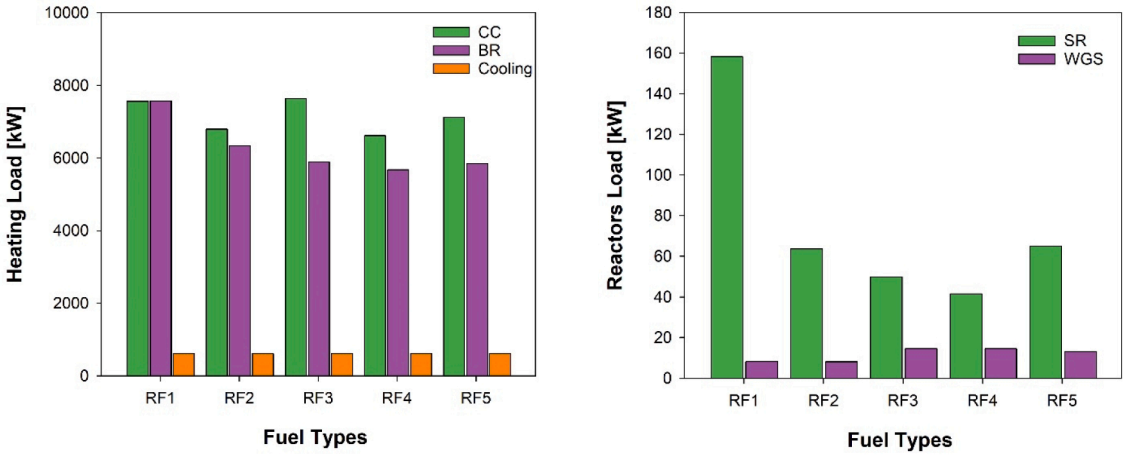

(a)Heating and cooling loads (b) Reactors loads

Fig. 4. Performance of the combustion chamber (CC), afterburner (BR) and cooling load (a) and the reactors SR and WGS (b) with respect to fuel blends.

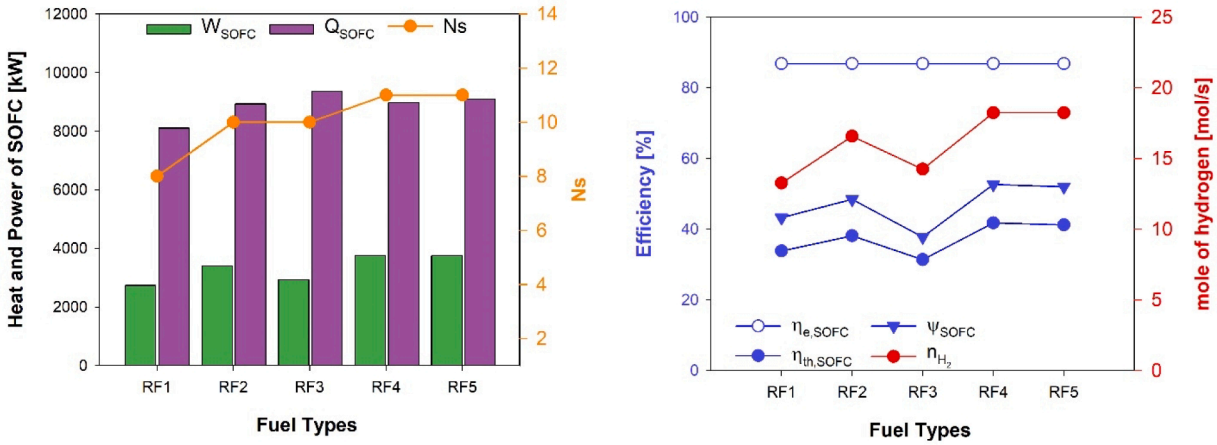

(a) Heat and power of the SOFC and number of stacks (b) Efficiencies and required hydrogen amount

Fig. 5. Performance of the SOFC: heat and power and number of stacks (a) and energetic and exergetic efficiencies and amount of required hydrogen [mol/s] (b).

Table 12
CO_2 emissions using diesel and sustainable fuels.

Emissions	Diesel	RF1	RF2	RF3	RF4	RF5
CO_2 [kg/s]	2.510	1.214	0.886	0.699	0.653	0.679
Reduction [%]	0	51.6	64.7	72.1	74.0	73.0

studied in the AEC + PEMFC system. Firstly, the effect of N1 (KOH solution) mass flowrate on the AEC performance is studied under the N2 equals 0.5 kg/s and illustrated in Fig. 7. Increasing the N1 mass flowrates from 0 to 30 kg/s increases the required power from 0 to 13 MW and increases the rejected heat from 0 to 33 MW, and consequently

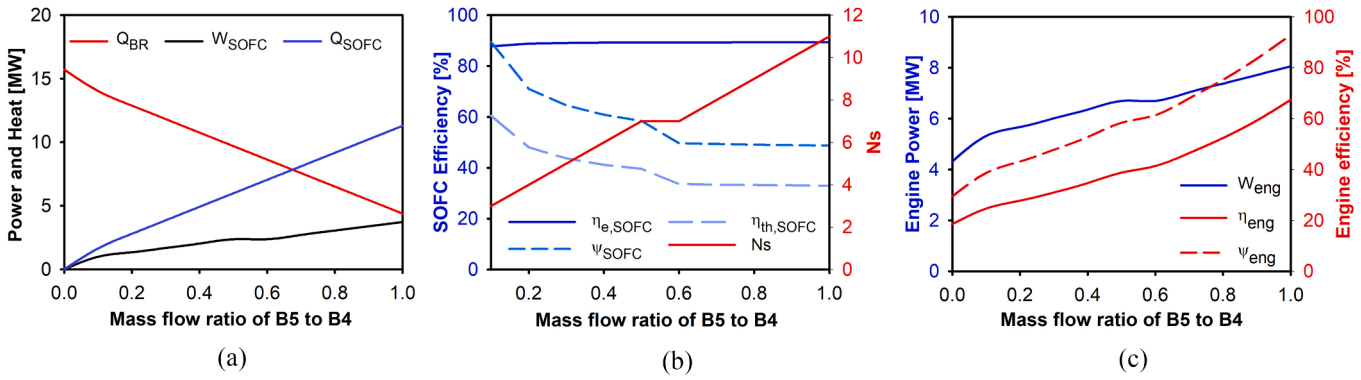

Fig. 6. Effect of SP1 ratios on power and heat of the BR and SOFC (a), efficiencies and number of stacks (b), and (c) engine power and overall efficiencies.

increases the number of stacks from 0 to 110 stacks, as shown in Fig. 7-b to increase hydrogen amount from 1.66 mol/s to 94.5 mol/s. However, the thermal efficiency of the AEC improves by increasing the N1 mass flowrates from 0 to 3 kg/s and remains constant after that, as shown in Fig. 7-b. However, the exergetic efficiency decreases from 50 to 38% during 0 to 3 kg/s and remains constant.

Secondly, maintaining the N1 to be 0.5 kg/s while changing the N_2 (NH_3 solution) mass flowrates is investigated and displayed in Fig. 8. Changing the N2 mass flowrates from 0 to 30 kg/s increases the required power from 0 to 6 MW, rejected heat from 0 to 25 MW, and a number of stacks from 0 to 52, as shown in Fig. 8-a to increase hydrogen amount from 1.66 mol/s to 43 mol/s. This decreases the AEC performance by 20% in thermal efficiency and 60% in exergetic efficiency through changing the mass flowrates from 0 to 3 kg/s, but after that the efficiencies remain constant, as shown in Fig. 8-b.

Thirdly, 11 cases are selected to consider changing N1, N2, and A1 simultaneously, starting from 0.5 to 10 kg/s for N1 and N2 and 0.02 to 0.3 kg/s for A1, as shown in Fig. 9. Increasing the mass flowrates increases the required power of the AEC from 0.35 to 5.9 MW and its number of stacks from 3 to 50 stacks, and generated power of the PEMFC from 0.34 to 6.1 MW and its number of stacks from 3 to 54 stacks, as shown in Fig. 9-a. The hydrogen amount increases from 2.5 mol/s (0.005 kg/s) in Case 1 to 42.5 mol/s (0.083 kg/s) in Case 11. The efficiencies of the PEMFC and AEC are plateau as the mass flow rates increases to be thermal efficiency of 90% and 76% for the PEMFC and AEC, respectively, and exergetic efficiency of 65% and 50% for the PEMFC and the AEC, respectively, as shown in Fig. 9-b.

The thermal and electrical efficiencies of the AEC do not change because the mass flow rates of N1 and N2 have parallelly increased with the same difference. Therefore, the AEC voltage loss remains unchanging for all cases reflecting on the constant electrical efficiency. In addition, the power and heat of the AEC vary as a straight line of constant slope, which equals the slope of increasing mass flowrates of ammonia and potassium hydroxide solutions of N1 and N2. This constant variation yields the constant thermal efficiency of the AEC for all cases.

The hydrogen amount needed for the hybrid engine is much higher and cannot fully account for the hydrogen production system since the hydrogen amounts are 73, 106, 121, 113, 113 mol/s for RF1 to RF5, respectively. To fully account for the hydrogen production, the AEC should be 200 stacks of total area of 4500 m^2 to 124 mol/s with total power of 17.7 MW, which is unrealistic to perform onboard a train to provide such amount per second. However, this production can be operated continuously during turn on and off of the engine to cover the need for hydrogen production. According to Case 1 where the number of stacks is 3 for each, the net power between the AEC and PEMFC is negative, meaning the power of the AEC requires more than the power of the PEMFC to be covered. However, starting from Case 2, the number of stacks for the PEMFC is higher than that of the AEC by 1 and increased to 4, resulting in increasing the power of the PEMFC more than the AEC so that the net power is positive of 90 kW for Case 2 and increased to about 225 kW for Case 11. The best option is to use Case 2 where the number of stacks is 6 for the PEMFC and 5 for the AEC and net power is 90 kW to produce 4.2 mol/s of hydrogen by the AEC, and an amount of 3.6 mol/s is used for the PEMFC and 0.6 mol/s (1.2 g/s or 4.32 kg/h) is stored in tanks.

4.2.4. *Effect of current density of fuel cells*

The current density of fuel cells is also considered in the study under the same active stack areas of 64 m^2 for SOFC and 30 m^2 for the AEC, and 15 m^2 for the PEMFC, as shown in Fig. 10. Increasing the current density from 0.1 to 1.0 A/cm^2 slightly affects the power of the AEC (about 428 kW) and PEMFC (about 243 kW), but it fluctuates the power of the SOFC and drops down from 3000 kW to 2500 kW, as shown in Fig. 10-a. The electric efficiencies of fuel cells decrease from 95% to 85% for the PEMFC and 95% to 78% for the SOFC while remaining constant for the

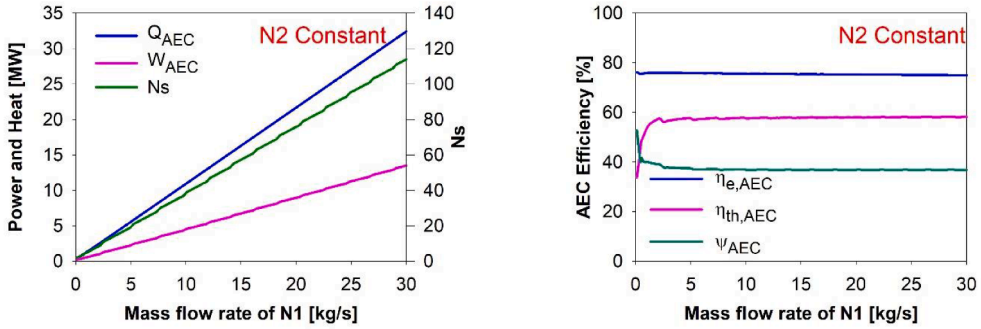

Fig. 7. Effect of N1 ($KOH + H_2O$) mass flowrates of AEC while N2 is constant: (a) heat, power, and number of stacks, and (b) overall efficiencies of AEC.

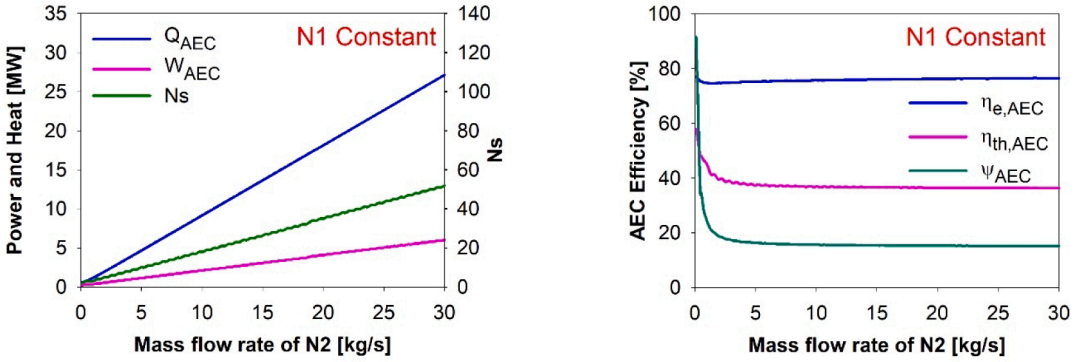

(a) Heat, power, and number of stacks of AEC (b) Overall efficiencies of AEC

Fig. 8. Effect of N2 ($NH_3 + H_2O$) mass flowrates of the AEC while N1 is constant: (a) heat, power, and number of stacks, and (b) overall efficiencies of the AEC.

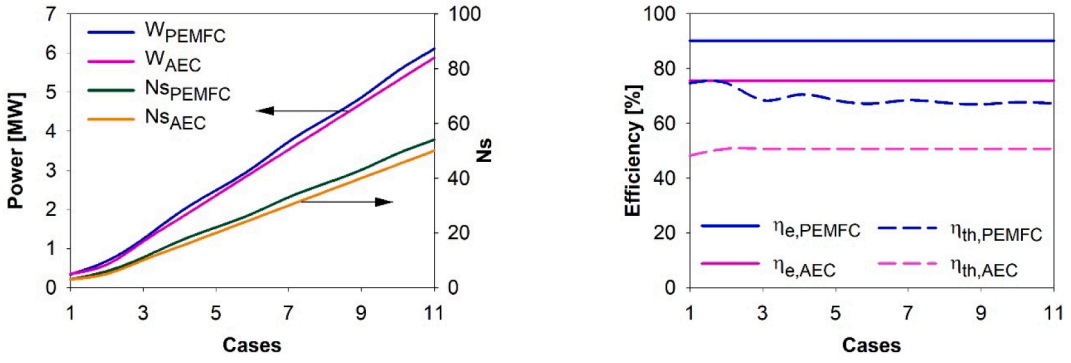

(a) Power and Ns of PEMFC and AEC (b) Efficiencies of PEMFC and AEC

Mass flowrate \ Cases	1	2	3	4	5	6	7	8	9	10	11
N1 (KOH-H_2O) [kg/s]	0.5	1	2	3	4	5	6	7	8	9	10
N2 (NH_3-H_2O) [kg/s]	0.5	1	2	3	4	5	6	7	8	9	10
A1 (O_2) [kg/s]	0.02	0.05	0.07	0.08	0.15	0.2	0.2	0.2	0.3	0.25	0.3

Fig. 9. Different cases of changing mass flowrates of N1, N2, and A1: (a) Power and number of stacks of the PEMFC and AEC, and (b) efficiencies of the PEMFC and AEC.

AEC. The thermal efficiencies behave as a sinusoidal wave since they are increased for the AEC from 70 to 80%, for 42% to 56% for the PEMFC, but they are decreased from 38% to 28% for the SOFC, as shown in Fig. 10-b. The number of stacks for all fuel cells exponentially decays from 26 to 3 for the AEC, 14 to 2 for PEMFC, and from 11 to 3 for the SOFC, as shown in Fig. 10-c.

4.2.5. Effect of constant cell area of fuel cells

In this subsection, we considered constant current density of 0.5 A/cm^2, constant active area of 0.64 m^2, and number of cells of 100 cells per a stack. Then, the fuel cells showed the performance as listed in Table 13. Therefore, the number of stacks will be 8 for the SOFC, 1 for the PEMFC, and 3 for the AEC. Also, the power will be about 2.7 MW for the SOFC, 0.3 MW for the PEMFC, and 0.5 MW for the AEC. These cases

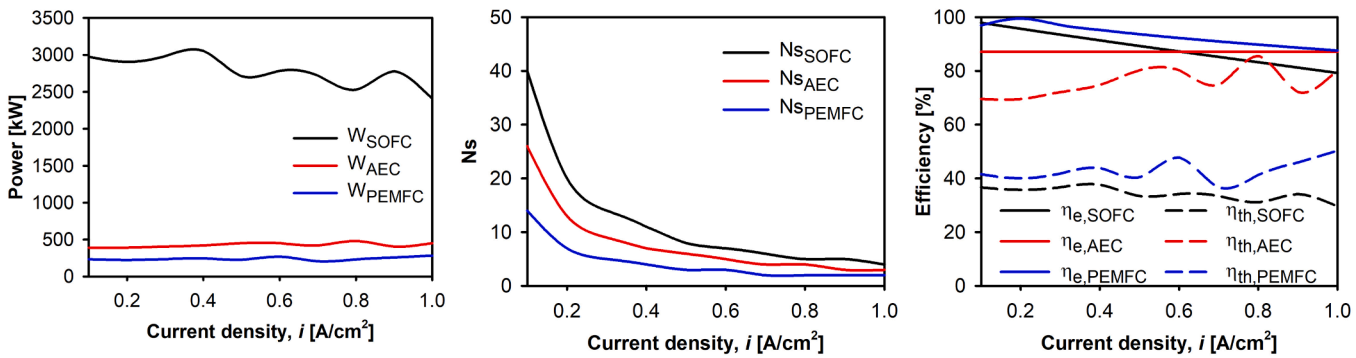

(a) Electric power of FCs (b) Efficiencies of FCs (c) Number of required stacks

Fig. 10. Effect of current density on fuel cell performance: (a) electric power, (b) thermal and electric efficiencies, and (c) number of required stacks.

Table 13
Fuel cell performances at equal current density and active cell area.

Parameter	Ns	A_t	$\dot{W}_{FC}$	$n_{H_2,cal}$	$n_{H_2,req}$
Unit	—	[m^2]	[kW]	[mol/s]	[mol/s]
SOFC	8	512	2713.3	13.27	12.95
PEMFC	1	64	324.2	1.66	1.02
AEC	3	192	482.4	3.32	2.55

can produce more hydrogen than needed about 13 mol/s for the SOFC, 2 mol/s for the PEMFC, and 3 mol/s for the AEC. That results in a negative net power (-158.2 kW) of hydrogen production yielding to lower the overall power of the engine from 7211.8 kW to 7053.6 kW for RF1.

5. Conclusions

This paper proposed a hybrid locomotive engine to replace the EMD 16–710-G3 used for Canada's rail transportation. The proposed hybrid engine combines a gas turbine with a fuel cell system and an energy recovery system. The engine counts on alternative fuels such as dimethyl ether, ethanol, hydrogen, methanol, and methane in the forms of five hydrogen-based fuel blends. The engine is simulated using Aspen Plus to investigate its performance thermodynamically. Some parametric studies are also conducted to understand the effects of different fuel blends, mass flow rates of the AEC and current density of the fuel cells. The following conclusions can be drawn from the study:.

- The hybrid locomotive engine can produce a total power of 7211.8 kW with 48% thermal efficiency and 51% exergy efficiency using RF1 (methane and hydrogen blend).
- Excluding the hydrogen production system, the overall engine power is a minimum of 6.8 MW using RF1 and a maximum of 7.9 MW using RF5 (all fuel blend).
- The energy recovery system includes the TG and ARS, which produce 925 kW of electrical power and 915 kW cooling load.
- The SOFC generates a minimum power of 3 MW using RF1 and RF3 (ethanol and hydrogen fuel blend) and a maximum of 3.75 MW using RF5.
- The CO_2 emissions are reduced by the designed system and fuel utilization to more than 70% compared to a traditional gas turbine with diesel fuel.
- The onboard hydrogen production using 6 stacks of the PEMFC and 5 stacks of the AEC can generate a positive net power of 90 kW and provide 4.32 kg/h hydrogen for storage.
- Increasing the current density from 0.1 to 1 A/cm^2 negatively affects the SOFC performance by reducing the power from 3000 kW to 2500 kW, but does not affect the power of the AEC and PEMFC.
- Increasing the current density from 0.1 to 1 A/cm^2 can reduce the number of stacks for all the fuel cells to less than 10.

CRediT authorship contribution statement

Shaimaa Seyam: Methodology, Software, Writing – original draft, Investigation, Visualization. **Ibrahim Dincer:** Supervision, Conceptualization, Funding acquisition, Writing – review & editing. **Martin Agelin-Chaab:** Supervision, Conceptualization, Funding acquisition, Writing – review & editing.

Declaration of Competing Interest

The authors declare that they have no known competing financial interests or personal relationships that could have appeared to influence the work reported in this paper.

Acknowledgement

The authors acknowledge the financial support provided by Transport Canada through its Clean Transportation Program - Research and Development and the Natural Sciences and Engineering Research Council of Canada (NSERC).

References

[1] Shah MI, Adedoyin FF, Kirikkaleli D. An evaluation of the causal effect between air pollution and renewable electricity production in Sweden: Accounting for the effects of COVID-19. Int J Energy Res 2021;45:18613–30. https://doi.org/10.1002/er.6978.
[2] Dincer I. COVID-19 coronavirus: Closing carbon age, but opening hydrogen age. Int J Energy Res 2020;44(8):6093–7.
[3] Nadi F, Özilgen M. Effects of COVID-19 on energy savings and emission reduction: A case study. Int J Glob Warm 2021;25:38–57. https://doi.org/10.1504/IJGW.2021.117432.
[4] Boretti A. Covid 19 impact on atmospheric CO2 concentration. Int J Glob Warm 2020;21:317–23. https://doi.org/10.1504/IJGW.2020.108686.
[5] Natural Resources Canada. Energy Fact Book 2021-2022. 2021.
[6] Vielstich W, Lamm A, Gasteiger HA. Handbook of Fuel Cells - Fundamentals, Technology and Applications. John Wiley & Sons, Ltd 2010. https://doi.org/10.1002/9780470974001.f500032.
[7] Haji Akhoundzadeh M, Panchal S, Samadani E, Raahemifar K, Fowler M, Fraser R. Investigation and simulation of electric train utilizing hydrogen fuel cell and lithium-ion battery. Sustain Energy Technol Assessments 2021;46:101234. https://doi.org/10.1016/j.seta.2021.101234.
[8] Sarma U, Ganguly S. Determination of the component sizing for the PEM fuel cell-battery hybrid energy system for locomotive application using particle swarm optimization. J Energy Storage 2018;19:247–59. https://doi.org/10.1016/j.est.2018.08.008.
[9] Seyam S, Dincer I, Agelin-Chaab M. Development and assessment of a cleaner locomotive powering system with alternative fuels. Fuel 2021;296:120529. https://doi.org/10.1016/j.fuel.2021.120529.
[10] Al-Hamed KHM, Dincer I. A novel ammonia solid oxide fuel cell-based powering system with on-board hydrogen production for clean locomotives. Energy 2021;220:119771. https://doi.org/10.1016/j.energy.2021.119771.
[11] Guo F, Qin J, Ji Z, Liu H, Cheng K, Zhang S. Performance analysis of a turbofan engine integrated with solid oxide fuel cells based on Al-H2O hydrogen production for more electric long-endurance UAVs. Energy Convers Manag 2021;235:113999. https://doi.org/10.1016/j.enconman.2021.113999.
[12] Little DJ, Smith MR, Hamann TW. Electrolysis of liquid ammonia for hydrogen generation. Energy Environ Sci 2015;8:2775–81. https://doi.org/10.1039/c5ee01840d.
[13] Dong BX, Ichikawa T, Hanada N, Hino S, Kojima Y. Liquid ammonia electrolysis by platinum electrodes. J Alloys Compd 2011;509:S891–4. https://doi.org/10.1016/j.jallcom.2010.10.157.
[14] Goshome K, Yamada T, Miyaoka H, Ichikawa T, Kojima Y. High compressed hydrogen production via direct electrolysis of liquid ammonia. Int J Hydrogen Energy 2016;41:14529–34. https://doi.org/10.1016/j.ijhydene.2016.06.137.
[15] Hanada N, Kohase Y, Hori K, Sugime H, Noda S. Electrolysis of ammonia in aqueous solution by platinum nanoparticles supported on carbon nanotube film electrode. Electrochim Acta 2020;341:136027. https://doi.org/10.1016/j.electacta.2020.136027.
[16] Luo D, Sun Z, Wang R. Performance investigation of a thermoelectric generator system applied in automobile exhaust waste heat recovery. Energy 2022;238:121816. https://doi.org/10.1016/j.energy.2021.121816.
[17] Alegria P, Catalan L, Araiz M, Rodriguez A, Astrain D. Experimental development of a novel thermoelectric generator without moving parts to harness shallow hot dry rock fields. Appl Therm Eng 2022;200:117619. https://doi.org/10.1016/j.applthermaleng.2021.117619.
[18] Ma X, Hu S, Hu W, Luo Y, Cheng H. Experimental investigation of waste heat recovery of thermoelectric generators with temperature gradient. Int J Heat Mass Transf 2022;185:122342. https://doi.org/10.1016/j.ijheatmasstransfer.2021.122342.
[19] Chen H, Huang Y, Chen Z, Jiang Y. Performance analysis of the system integrating a molten carbonate fuel cell and a thermoelectric generator with inhomogeneous heat conduction. Appl Therm Eng 2022;200:117729. https://doi.org/10.1016/j.applthermaleng.2021.117729.
[20] Seyam S, Dincer I, Agelin-Chaab M. Development and assessment of a cleaner locomotive powering system with alternative fuels. Fuel 2021;185:120529. https://doi.org/10.1016/j.applthermaleng.2020.116432.
[21] Turbines S. Centaur(R) 40: Gas Turbine Compressor Set. accessed February 12, 2022 A Caterp Co 2021:1–2. https://s7d2.scene7.com/is/content/Caterpillar/CM20150703-52095-02409.
[22] Midilli A, Akbulut U, Dincer I. A parametric study on exergetic performance of a YSZ electrolyte supported SOFC stack. Int J Exergy 2017;24:173–200. https://doi.org/10.1504/IJEX.2017.087653.
[23] Ji Z, Qin J, Cheng K, Guo F, Zhang S, Dong P. Thermodynamics analysis of a turbojet engine integrated with a fuel cell and steam injection for high-speed flight. Energy 2019;185:190–201. https://doi.org/10.1016/j.energy.2019.07.016.

[24] Xing L, Das PK, Song X, Mamlouk M, Scott K. Numerical analysis of the optimum membrane/ionomer water content of PEMFCs: The interaction of Nafion® ionomer content and cathode relative humidity. Appl Energy 2015;138:242–57. https://doi.org/10.1016/j.apenergy.2014.10.011.
[25] Boggs BK, Botte GG. On-board hydrogen storage and production: An application of ammonia electrolysis. J Power Sources 2009;192:573–81. https://doi.org/10.1016/j.jpowsour.2009.03.018.
[26] O'Hayre R, Cha S-W, Colella WG, Prinz FB. Fuel cell fundamentals. Third Edit. Hoboken, New Jersey: John Wiley & Sons Inc.; 2016.
[27] Seyam S, Dincer I, Agelin-Chaab M. Investigation of Two Hybrid Aircraft Propulsion and Powering Systems Using Alternative Fuels. Energy 2021;232:121037. https://doi.org/10.1016/j.energy.2021.121037.
[28] Schröder M, Becker F, Kallo J, Gentner C. Optimal operating conditions of PEM fuel cells in commercial aircraft. Int J Hydrogen Energy 2021;46:33218–40. https://doi.org/10.1016/j.ijhydene.2021.07.099.
[29] Carmo M, Fritz DL, Mergel J, Stolten D. A comprehensive review on PEM water electrolysis. Int J Hydrogen Energy 2013;38:4901–34. https://doi.org/10.1016/j.ijhydene.2013.01.151.
[30] Kocer AA, Ozturk M. Thermodynamic analysis of power and hydrogen production from renewable energy-based integrated system. Int J Exergy 2016;19:519–43. https://doi.org/10.1504/IJEX.2016.075883.
[31] Godula-Jopek A. Hydrogen Production by Electrolysis. Weinheim, Germany: Wiley-VCH Verlag GmbH & Co.; 2015.
[32] Fernández-Yáñez P, Romero V, Armas O, Cerretti G. Thermal management of thermoelectric generators for waste energy recovery. Appl Therm Eng 2021;196:117291.
[33] Wilbrecht S, Beitelschmidt M. The Potential of a Cascaded TEG System for Waste Heat Usage in Railway Vehicles. J Electron Mater 2018;47:3358–69. https://doi.org/10.1007/s11664-018-6094-z.
[34] Xuan XC, Ng KC, Yap C, Chua HT. The maximum temperature difference and polar characteristic of two-stage thermoelectric coolers. Cryogenics (Guildf) 2002;42:273–8. https://doi.org/10.1016/S0011-2275(02)00035-8.
[35] Meddad M, Eddiai A, Farhan R, Benahadouga S, Mazroui M, Rguiti M. Design hybridization system of TEG/PZT for power generation: Modelling and experiments. Superlattices Microstruct 2019;127:86–92. https://doi.org/10.1016/j.spmi.2018.03.007.
[36] Seyam S. Energy and Exergy Analysis of Refrigeration Systems. Low-temperature Technol, IntechOpen 2019:13. https://doi.org/10.5772/57353.
[37] Dincer I. Refrigeration system and application. Third Edit. West Sussex, UK: Wiley & Sons Ltd; 2017.
[38] Wei S, Yu M, Pei B, Ma Z, Li S, Kang Y. Effect of hydrogen enrichment on the laminar burning characteristics of dimethyl-ether/methane fuel: Experimental and modeling study. Fuel 2021;305:121475. https://doi.org/10.1016/j.fuel.2021.121475.
[39] Chen H, He J, Chen Z, Geng L. A comparative study of combustion and emission characteristics of dual-fuel engine fueled with diesel/methanol and diesel–polyoxymethylene dimethyl ether blend/methanol. Process Saf Environ Prot 2021;147:714–22. https://doi.org/10.1016/j.psep.2021.01.007.
[40] Wang H, Fang R, Weber BW, Sung CJ. An experimental and modeling study of dimethyl ether/methanol blends autoignition at low temperature. Combust Flame 2018;198:89–99. https://doi.org/10.1016/j.combustflame.2018.09.012.
[41] Badwal SPS, Giddey S, Kulkarni A, Goel J, Basu S. Direct ethanol fuel cells for transport and stationary applications - A comprehensive review. Appl Energy 2015;145:80–103. https://doi.org/10.1016/j.apenergy.2015.02.002.
[42] Semelsberger TA, Borup RL, Greene HL. Dimethyl ether (DME) as an alternative fuel. J Power Sources 2006;156:497–511. https://doi.org/10.1016/j.jpowsour.2005.05.082.
[43] Matzen M, Demirel Y. Methanol and dimethyl ether from renewable hydrogen and carbon dioxide: Alternative fuels production and life-cycle assessment. J Clean Prod 2016;139:1068–77. https://doi.org/10.1016/j.jclepro.2016.08.163.
[44] Yuan W, Frey HC, Wei T, Rastogi N, VanderGriend S, Miller D, et al. Comparison of real-world vehicle fuel use and tailpipe emissions for gasoline-ethanol fuel blends. Fuel 2019;249:352–64.
[45] AspenTech. Aspen Physical Property System: Physical property data 11 . 1. Cambridge, USA: Aspen Technology Inc.; n.d.
[46] Ma Q, Zhang Q, Chen J, Huang Y, Shi Y. Effects of hydrogen on combustion characteristics of methane in air. Int J Hydrogen Energy 2014;39:11291–8. https://doi.org/10.1016/j.ijhydene.2014.05.030.
[47] Yoon W, Park J. Parametric study on combustion characteristics of virtual HCCI engine fueled with methane–hydrogen blends under low load conditions. Int J Hydrogen Energy 2019;44:15511–22. https://doi.org/10.1016/j.ijhydene.2019.04.137.
[48] Tian Z, Wang Y, Zhen X, Liu D. Numerical comparative analysis on performance and emission characteristics of methanol/hydrogen, ethanol/hydrogen and butanol/hydrogen blends fuels under lean burn conditions in SI engine. Fuel 2022;313:123012. https://doi.org/10.1016/j.fuel.2021.123012.
[49] Londerville S, Colannino J, Baukal CE. Combustion fundamentals. John Zink Hamworthy Combust Handbook, Second Ed Vol 1 - Fundam 2012:79–124. doi:10.1201/b11619.